A digital twin to quantitatively understand aging mechanisms coupled effects of NMC battery using dynamic aging profiles

Guo, Wendi; Li, Yaqi; Sun, Zhongchao; Vilsen, Søren Byg; Stroe, Daniel Ioan

Published in:
Energy Storage Materials

DOI (link to publication from Publisher):
10.1016/j.ensm.2023.102965

Publication date:
2023

Document Version
Publisher's PDF, also known as Version of record

Energy Storage Materials 63 (2023) 102965

Contents lists available at ScienceDirect

Energy Storage Materials

journal homepage: www.elsevier.com/locate/ensm

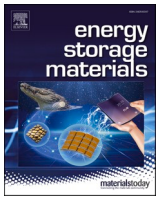

A digital twin to quantitatively understand aging mechanisms coupled effects of NMC battery using dynamic aging profiles

Wendi Guo [a], Yaqi Li [a,b,*], Zhongchao Sun [a,*], Søren Byg Vilsen [c], Daniel Ioan Stroe [a]

[a] AAU Energy, Aalborg University, Aalborg 9220, Denmark
[b] Department of Materials and Production, Aalborg University, Aalborg 9220, Denmark
[c] Department of Mathematical Sciences, Aalborg University, Aalborg 9220, Denmark

ARTICLE INFO

Keywords:
Digital twin
Aging mechanisms
NMC battery
Dynamic aging profiles
Charging protocols

ABSTRACT

Traditional lithium-ion battery modeling does not provide sufficient information to accurately verify battery performance under real-time dynamic operating conditions, particularly when considering various aging modes and mechanisms. To improve the current methods, this paper proposes a lithium-ion battery digital twin that can capture real-time data and integrate the strong coupling between SEI layer growth, anode crack propagation, and lithium plating. It can be utilized to estimate aging behavior from macroscopic full-cell level to microscopic particle level, including voltage-current profiles in dynamic aging conditions, predict the degradation behavior of Nickel-Manganese-Cobalt-Oxide (NMC) based lithium-ion batteries, and assist in electrochemical analysis. This model can improve the root cause analysis of cell aging, enabling a quantitative understanding of aging mechanism coupled effects. Three charging protocols with dynamic discharging profiles are developed to simulate real vehicle operation scenarios and used to validate the digital twin, combining operando impedance measurements, post-mortem analysis, and SEM to further prove the conclusions. The digital twin can accurately predict battery capacity fade within 0.4% MAE. The results indicate that SEI layer growth is the primary contributor to capacity degradation and resistance increase. Based on the analysis of the model, it is concluded that one of the proposed multi-step charging protocols, in comparison to a standard continuous charging protocol, can reduce the degradation of NMC-based lithium-ion batteries. This paper represents a firm physical foundation for future physics-informed machine learning development.

1. Introduction

Owing to their high energy density and high charging efficiency, lithium-ion batteries (LiBs) are widely used in electric vehicles (EVs) and renewable energy storage for our low-carbon society. Market Research Future [1] has projected significant growth in the LiBs market for EVs, with a healthy compound annual growth rate (CAGR) of over 18 % by the year 2030. Given the rapid development of EVs, ensuring battery reliability has become a major concern. The challenge of estimating and extending the LiBs' effective lifetime lies in the strong coupling with the operating conditions (such as temperature, loading, and SOC range) and intrinsic factors (such as chemistry and geometry factors) [2,3]. LiBs, as energy storage devices, undergo electrochemical reactions that involve lithium-ion intercalation and delamination in the electrodes, driving mechanical effects such as volume expansion and contraction of active particles. Moreover, lithium plating can occur during fast charging, resulting in significant capacity fade when lithium ions cannot be inserted into active particles but deposit lithium metal on the particle surface [4]. To accurately predict the aging behavior of LiBs under dynamic operating conditions and design optimized charging protocols, it is essential to couple multiphysics factors [5] and quantify the effects of different aging mechanisms.

During the LiBs aging process, solid electrolyte interphase (SEI) layer growth is regarded as the main aging mechanism leading to capacity fade and resistance increase [6]. Solvent molecules accompanying lithium ions traverse the SEI layer and undergo irreversible reactions with neutral lithium interstitial atoms or lithium compounds on the graphite surface, forming interfacial film substances. These processes contribute to the irreversible capacity fade [7]. The capacity fade induced by SEI layer growth exhibits an asymptotic linear shift in long-term capacity retention [8]. The process of thickening the SEI layer further depletes the lithium ions, solvents, and salts, increasing the

* Corresponding author at: AAU Energy, Aalborg University, Aalborg 9220, Denmark.
E-mail addresses: yaqili@mp.aau.dk (Y. Li), zs@energy.aau.dk (Z. Sun).

https://doi.org/10.1016/j.ensm.2023.102965
Received 15 June 2023; Received in revised form 14 August 2023; Accepted 11 September 2023
Available online 25 September 2023

internal resistance, and ultimately leading to a loss in its capacity; however, coupling the SEI layer growth with other aging mechanisms will cause a non-linear capacity drop. The mechanical fatigue of electrodes has been considered to be an essential part of LiBs' capacity degradation mode [9]. In addition, under high current [10] or low-temperature conditions [11], lithium metal deposition further accelerates the increase of the electrolyte potential gradient in the anode, which increases the lithium plating rate and changes the degradation behavior from linear to nonlinear. Although the coupling of different side reactions in LiBs is not a novel concept, there is currently a lack of comprehensive digital twin models that integrate real-time dynamic profiles and account for the strong coupling and mutual feedback among all side reactions. Such models are crucial for characterizing performance degradation in terms of capacity, energy, resistance, and electrochemical analysis. Additionally, the lack of models capable of accurately quantifying the coupling and decomposition effects of all relevant mechanisms, as well as facilitating the development of charging protocols, further highlights this research gap. Furthermore, it is noteworthy that existing models have not been rigorously validated by closed-loop experiments to ensure their reliability and suitability for practical applications.

Previous research has attempted to understand the behaviour of LiBs through two physical domain coupling, which involves the study of interactions between multiscale, including the particle level, electrode level, and full cell level. One such area is electrochemical-mechanical coupling. The expansion and contraction of graphite particles during lithiation and delithiation induce stresses that drive the creation and growth of anode cracks [12]. Additionally, these cracks contribute to the formation of the extended SEI layer, further trapping the cyclable lithium ions and resulting in capacity fade over time [13]. Tests and simulations have demonstrated that Li-ion batteries charged while experiencing mechanical constraints exhibit faster reaching of the cut-off voltage [14]. In addition, studies focusing on the mechanical properties of the electrode's active material [15], as well as the external mechanical stress [14], reported that both factors can significantly impact the state of health (SOH) of the battery, reducing its lifetime. Meanwhile, changes in cathode volume are mainly caused by lithium-ion extraction and insertion during charging and discharging, leading to observations of planar gliding microcracks in the nickel-rich cathodes of NMC cells [16]. The other area is electrochemical-thermal coupling. In this case, the non-uniform temperature distribution within the cell volume affects the electrochemical reaction rate. Additionally, the current density of the electrochemical reaction affects the thermal behavior of the cell [17]. Electrochemical reactions typically produce heat from various sources, including reaction heat, ohmic heat at the electrodes and collectors, and polarization heat of the active material at the interface. These heat sources drive average temperature changes, which, in turn, can influence the electrochemical reaction through temperature feedback. Recent studies have highlighted the significant impact of both excessive charging current [18] and ambient temperature [19] on the thermal behavior of batteries. However, all the aforementioned models lack a quantitative description of closed-loop validation utilizing real-time dynamic profiles.

In recent years, some studies have explored the coupling of electrochemical, mechanical, and thermal effects in batteries. Due to the significant increase in computational complexity, the coupling of these three fields is typically achieved using weak one-way coupling. For example, the mechanical strain energy generated by the lithium-ion intercalation reaction during electrochemical processes can cause cathode material loss, but there is no feedback loop between material loss and electrochemical reaction [20]. Other studies have attempted to establish strong coupling conditions. For instance, mechanical loading provides the geometric shape deformation and boundary conditions for electrochemical and thermal effects, which can be used to describe changes in the charging-discharging curves and temperature response [14]. The topology of the microstructure between particles can also create different mechanical stress distributions, and the non-uniform stress at the particle contact interface can affect the diffusion behaviour of lithium ions [21]. Multi-physics coupled multi-scale models are mainly aimed at battery design optimization and guiding the development of next-generation batteries [22], but are computationally burdensome for industrial applications to rapidly predict degradation behaviour, and develop charging protocols.

To fill in the blank and achieve the goal of capturing real-time data and accurately predicting the degradation behaviour, quantifying different mechanisms coupling and decomposition effects, and getting an optimized charging protocol, it is inevitable to consider the multi-physics interactions that affect battery behaviour in real-world applications. The real-world applications also indicate the necessity of designing dynamic tests that simulate real vehicle operation, as the majority of current studies still rely on standard constant-current constant-voltage (CCCV) charging and discharging profiles. Meanwhile, the complexity of these interactions makes it challenging to couple multi-scale modeling while considering actual particle morphology, significantly increasing the computational complexity. Balancing physical interpretability and computational complexity is crucial in practical engineering applications. The development of digital twin, which is strongly mechanisms coupled and experimentally validated, represents a crucial research endeavour to bridge the knowledge gap in the field of lifetime prediction, mechanisms quantification [23], and charging protocol development. Additionally, promising predictive models that integrate artificial intelligence hold significant potential for enhancing the flexibility, and generalizability of digital twin in the future [24], [25],[26].

In this study, a closed-loop digital twin framework through COMSOL Multiphysics 6.1 is constructed to investigate the strong coupling between SEI growth, anode crack propagation, and lithium plating mechanisms. To better describe the effect of the SEI structure, an outer organic layer, and an inner inorganic layer structure are created. Sensitivity parameters are refined through calibration using electrode particle size distributions, as well as charging-discharging voltage and current data. Three charging protocols (i.e., 1C CCCV, 2C CCCV, and MCCCV) with dynamic discharging profiles were designed to simulate real vehicle operation scenarios based on our previous work [27]. Through conducting aging tests and operando impedance measurements on NMC-based LiBs, a battery dataset is collected for predicting aging behavior. The mechanisms coupled effects under the three aging conditions are quantitatively analysed using the digital twin. Post-mortem analysis further confirms the formation of SEI films and cracking under the three charging protocols, but no lithium dendrite is observed. Interestingly, the aging behaviour for the MCCCV protocol is slowed down and no rapid nonlinear degradation is observed, making it a potential charging protocol for EVs. The digital twin proposed in this study will also become an important physical foundation in future physics-informed machine learning algorithms.

2. Method

The overall framework of this study is illustrated in Fig. 1. Based on aging tests and measured battery parameters, a proposed digital twin is employed to accurately quantify battery aging behaviour, encompassing three considered aging mechanisms. Furthermore, leveraging the insights gained from this digital twin, a charging profile is proposed to optimize the NMC battery's service life. The most significant step is to build a digital twin for the considered LiBs. To better describe the coupling effects of SEI layer growth, cracking, and Li plating, the following hypotheses about the modeling process are made.

- The particles of the cathode and anode active materials are assumed to be spherical.
- The porous SEI layer is uniformly wrapped around the anode/graphite surfaces and is of uniform thickness.

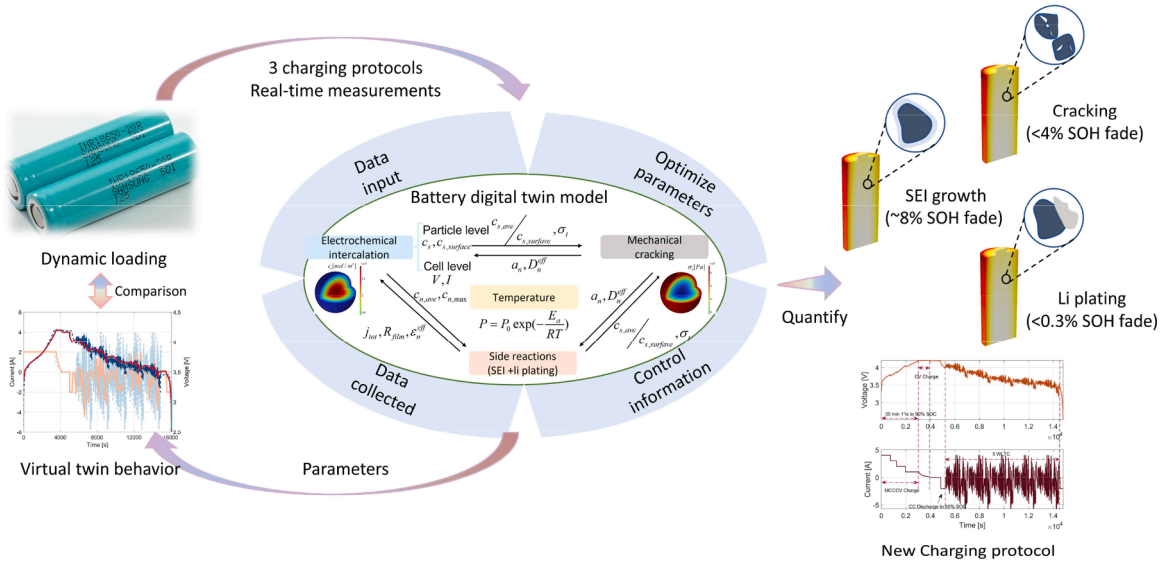

Fig. 1. Overview of the quantification for NMC battery aging based on the digital twin process related to different aging mechanisms coupling and perspectives for extended cycle life.

- SEI layer growth occurs mostly in the stable inner inorganic layer because the organic layer can be moved or further reduced [6].
- The initial cracks are identical and equally distributed on the surface of the graphite particles. The cracks only extend towards the inner particle, and the crack length and density are constant.
- The maximum diffusion-induced cyclic tangential stress caused by the intercalation and deintercalation of lithium ions acts as the source of crack propagation and continues to act on the graphite surface.
- Li stripping evolution is not considered.
- Thermal effects are included via temperature-dependent material and diffusion coefficients.

2.1. Digital twin model description

Based on the pseudo-two-dimensional (P2D) model, a physics model is developed to investigate the degradation behaviour of NMC-based LiBs. The model developed here is based on our previous electrochemical-mechanical model [28], modified to consider the coupled effects of bilayer SEI structural growth, lithium plating, and crack propagation on the anode particles.

Fig. 2(a) illustrates an overview of modeling electrochemical main reactions and parasitic reactions. When discharging, the basic reaction process is the current flows out of the cathode and the outer circuit electrons move in the cathode. The lithium ions from the inner anode particles deintercalated, and the electrons flow directly into the current collector. As for parasitic reactions, (1) SEI layer can be completely produced under rapid kinetics before the start of the deintercalation, with potential in the range of 0~0. 25 V vs. Li+/Li. Electrolyte solvent molecules ethylene carbonate (EC) [29] can diffuse through the porous outer layer and tunnel with lithium ions and electrons in graphite, leading to the thickening of the existing SEI layer; (2) lithium plating can only occur when the overpotential of the reaction reaches below 0V vs. Li/Li+ [11]; (3) lithium ions de/intercalation can cause anode exfoliation during graphite contraction/expansion. The additional SEI layer will reform and cover the newly exposed surface, as shown in Fig. 2(b).

2.2. Main intercalation reaction

The desired main Li+ intercalation or deintercalation reaction happens on the particle surface, following the Butler-Volmer Equation as:

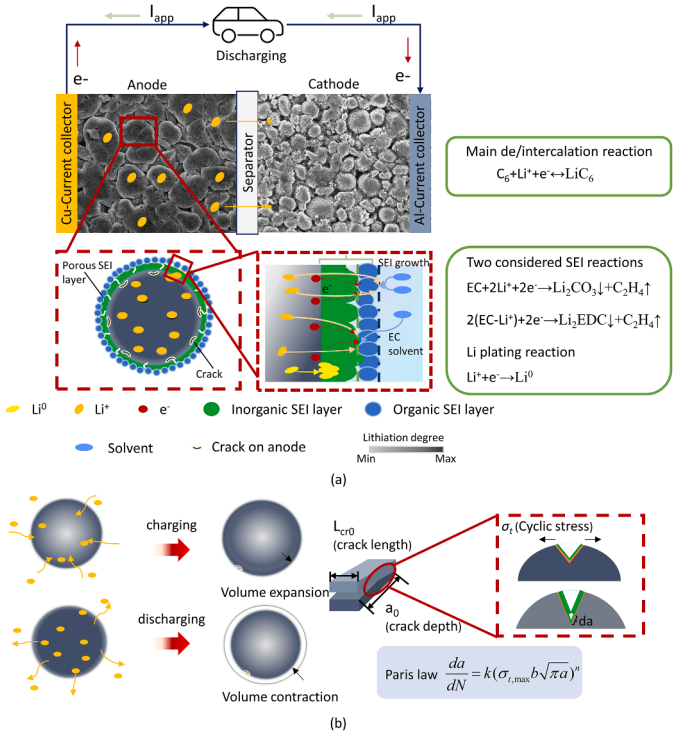

Fig. 2. (a) Modeling of electrochemical main reactions and parasitic reactions; (b)volume expansion and contraction to cause crack propagation.

$$j_{\text{int}} = j_{\text{int},0}\left[\exp\left(\frac{\alpha_a F}{RT}\eta_{\text{int}}\right) - \exp\left(\frac{(1-\alpha_a)F}{RT}\eta_{\text{int}}\right)\right] \quad (1)$$

where $j_{int,0}$ is the exchange current density, α_a is the anodic transfer coefficient, and η_{int} denotes the overpotential of the Li+ interpolation or de-interpolation reaction, given by

$$\eta_{\text{int}} = \phi_s - \phi_e - U_{ref} - j_{tot}R_{film} \quad (2)$$

where ϕ_s and ϕ_e are solid phase and electrolyte phase potential, U_{ref} is

the open circuit voltage (OCV), and R_{film} is the resistance of SEI film on graphite particles.

When the side reaction occurs at the negative electrode interface, the reaction rate needs to be modified by adding the additional rate induced by side reactions. The total current density j_{tot} is composed of the intercalation current j_{int}, the SEI formation current j_{SEI}, and the lithium plating current j_{lpt}: $j_{tot} = j_{int} + j_{SEI} + j_{lpt}$.

2.2.1. SEI layer growth

The SEI layer forms at the end of the first LiB cycle, the initial thickness of the inner inorganic and outer organic layers are constructed as follows.

$$l_0^{inorganic} = \frac{\delta Q_1 M_{SEI}^{inorganic}}{2A_0 \rho_{SEI}^{inorganic} F}$$
$$l_0^{organic} = \frac{(1-\delta) Q_1 M_{SEI}^{organic}}{2A_0 \rho_{SEI}^{organic} F} \quad (3)$$

where A_0 is the ideal value of the initial anode particle surface:

The SEI layer is positioned at the interface between the anode and the electrolyte. The graphite particles' expansion during charging generates fractures in the microporous SEI layer, and the cracks facilitate the formation of new SEI layer [30]. Thus, the current density of the SEI side reaction is as follows:

$$j_{SEI} = -\left[1 + HK_{crd}\left(\frac{C_{n,av}}{C_{n,\max}}\right)\right] \frac{J j_{1c,loc} C_{rate}}{\exp\left(\frac{\alpha_a F}{RT}\eta_{SEI}\right) + \frac{Q_{SEI} f J}{j_{1c,loc}}} \quad (4)$$

where J, H, and f are lumped parameters denoting the dimensionless exchange current, graphite relative expansion factor, and frequency, respectively [31], K_{crd} is the volume expansion factor related to the stoichiometric coefficient (denoted by $C_{n,av}/C_{n,max}$) in $LixC_6$, the over potential η_{SEI} of the SEI reaction is defined as $\eta_{SEI} = \Phi_s - \Phi_e - U_{eq,SEI}$ with the equilibrium potential $U_{eq,SEI}$ of SEI reaction set as 0.4 V, $J_{1c,loc}$ is local current density using 1 C charge/discharge current:

$$j_{1c,loc} = \frac{Q_0}{A_v \cdot L_n} \quad (5)$$

where Q_0 can be calculated as: $Q_0 = C_{p,max}(x_{p,max} - x_{p,min})\varepsilon_{s,p} L_p F$, A_v is the specific surface area denoted by $A_v = 3\varepsilon_n / r_n$.

The concentration of SEI film C_{SEI} formed on the anode can be calculated by mass conservation as $\partial C_{SEI} / \partial t = -A_v j_{SEI} / 2F$. The capacity fade Q_{SEI} (Ah/m^2) due to SEI layer growth is given as:

$$Q_{SEI} = \frac{\int_{negative} C_{SEI} \cdot F}{3600} \quad (6)$$

2.2.2. Lithium plating

It is assumed that lithium ions loss due to lithium plating is irreversible. Furthermore, in the following it is assumed that lithium stripping situation is neglected while discharging. Thus, the Tafel equation (instead of the Butler Volmer equation) can be used to describe the current density of the lithium deposition reaction as:

$$j_{lpt} = \begin{cases} -j_{lpl,0} \exp\left(-\frac{\alpha_{a,lpl} F}{RT}\eta_{lpl}\right), \eta_{lpl} \le 0 \\ 0, \eta_{lpl} > 0 \end{cases} \quad (7)$$

where $j_{lpl,0}$ is lithium plating current density at the anode particle interface given as and η_{lpl} is the overpotential of triggering lithium plating reaction given as $j_{lpl,0} = k_{lpl} c_l^{\alpha_{lpl}}$ and $\eta_{lpl} = \Phi_s - \Phi_e - j_{tot} R_{film}$, respectively.

The concentration of deposited lithium C_{lpt} can be calculated by mass conversation as: $\partial C_{lpt} / \partial t = -A_v j_{lpt} / F$ The capacity fade Q_{lpt} (Ah/m^2) due to lithium-plating is as follows, under the assumption that lithium plating is irreversible:

$$Q_{lpt} = \frac{\int_{negative} C_{lpt} \cdot F}{3600} \quad (8)$$

2.2.3. Crack formation of anode

We assume initial cracks in the anode's particles that serve as the cracking seeds when calculating the area of the SEI layer, the Initial cracks on the anode surface propagate under cycling conditions due to lithium ions diffusion-induced stress. These cracks leave the surface exposed to the electrolyte, and in turn, the SEI layer can be generated continuously. Paris' law describes how the crack length increases with the number of cycles N [32].

$$\frac{da}{dN} = k\left(\sigma_{t,\max} b\sqrt{\pi a}\right)^n \quad (9)$$

where k, b, and n are material-dependent constants, a is the crack depth, and $\sigma_{t,max}$ is the amplitude of diffusion-induced tangential stress at the anode particle surface.

The maximum tangential stress on the particle's surface is utilized to determine the crack growth. We consider the chemo-mechanical stresses induced by the diffusion of lithium ions within a spherical particle of radius R [33]. The body of the spherical particle is an isotropic, linearly elastic solid, and the tangential stress can be represented as:

$$\sigma_t(r_n, t) = \frac{E\Omega}{9(1-\nu)}\left[3C_{n,av}(r_n, t) - 3C_n(r_n, t)\right] \quad (10)$$

where E is Young's modulus, ν is Poisson's ratio, Ω is the solute's partial molar volume, $C_{n,av}(R)$ is the average concentration in a spherical volume of radius R, denoted as $C_{n,av}(r_n, t) = 3/r_n^3 \int_0^{r_n} r^2 C_n(r) dr$, and $C_n(R)$ is the concentration on the particle surface.

$$\frac{dA_{cr}}{dN} = 8\pi r_n^2 \rho_{cr} l_{cr,0} k\left(\sigma_{t,\max} b\sqrt{\pi a_0}\right)^n \left(\frac{2-n}{2} k\left(\sigma_{t,ampl} b\sqrt{\pi a_0}\right)^n N a_0^{\frac{n-2}{2}} + 1\right)^{\frac{n}{2-n}} \quad (11)$$

where r_n is the anode particle radius, ρ_{cr} is the number of cracks per particle unit area, $l_{cr,0}$ is the initial crack width, a_0 is the initial crack depth, N is the cycle number, and k is the reaction rate satisfied by Arrhenius law, expressed as $k = k_0 \exp(-E_{a,crack} / RT)$.

The crack propagation can affect the diffusion coefficient of the anode; The deeper the crack propagates, the smaller the effective diffusion constant for anode's active material:

$$D_n^{eff}(N) = D_{n,0}\left(1 - \frac{a(N)}{a_{\max}}\right)^{\beta} \quad (12)$$

where β is a fitting parameter, and a_{max} is the maximum limit of anode cack damage given [34]:

$$a_{\max} = -0.5902 \times \frac{0.7173 + 0.0027 \times r_n - 0.15/r_n}{1 + |0.0223 \times C_{rate} - 10.2115 - 0.002 \times r_n|} \quad (13)$$

The mechanical stress-related capacity loss can be divided into two parts: (1) capacity loss due to the SEI formation on the newly exposed surface, denoted by Q_{crack}, and (2) the SEI will also continue to grow to deplete capacity in cycles after the newly exposed area has been entirely covered, denoted by Q_{reform}.

The freshly exposed electrode surface will be entirely covered by SEI layer of thickness l_{SEI}^0 in one cycle ($dN = 1$). As a result, the capacity loss on the newly exposed surface is given as:

$$\frac{dQ_{crack}}{dN} = \frac{2 l_0^{inorganic} \rho_{SEI}^{inorganic} F}{\delta_e M_{SEI}^{inorganic}} \frac{dA_{cr}}{dN} \quad (14)$$

At the end of the i^{th} aging cycle, the exposed surface area due to crack propagation will form the SEI layer, which will continue to grow in the subsequent N-i cycles. As a result, the SEI reformation-induced capacity

loss in the cracked region in the N^{th} cycle can be stated as:

$$\frac{dQ_{reform}}{dN} = \frac{2\rho_{SEI}^{inorganic} F}{\delta_e M_{SEI}^{inorganic}} \sum_{i=1}^{N-1} \left(\frac{dA_{cr}}{dN}\right)_i \left(\frac{dl_{SEI}^{inorganic}}{dN}\right)_{N-i} \tag{15}$$

where $l_{SEI}^{inorganic}$ is the total inorganic SEI layer thickness expressed as:

$$\frac{dl_{SEI}^{inorganic}}{dN} = \frac{1}{2} K_{SEI,0} \exp\left(-\frac{E_{a,SEI}}{RT}\right) N^{-\frac{1}{2}} \tag{16}$$

where $K_{SEI,0}$ is the initial SEI growth reaction rate coefficient, and the SEI growth reaction rate follows the Arrhenius law with activation energy $E_{a,SEI}$.

Given that a crack has not yet grown in the first cycle, as only the initial formation of SEI happens, the equations for Q_{crack} and Q_{reform} can be solved by integration.

$$Q_{crack}(N) = \frac{2-n}{2} \frac{\Psi}{Z} \left[(1+ZN)^{\frac{2}{2-n}} - (1+Z)^{\frac{2}{2-n}}\right] \tag{17}$$

$$Q_{reform}(N) = \frac{K_{SEI,0} \exp\left(-\frac{E_{a,SEI}}{RT}\right) \Psi}{l_0^{inorganic}} \sum_{j=1}^{N-1} (1+Zj)^{\frac{n}{2-n}} (N-j)^{\frac{1}{2}} \tag{18}$$

where

$$\psi = \frac{16\pi r_n^2 \rho_{cr} l_{cr,0} k \left(\sigma_{t,\max} b \sqrt{\pi a_0}\right)^n \rho_{SEI}^{inorganic} F l_0^{inorganic}}{\delta_e M_{SEI}^{inorganic}} \tag{19}$$

and

$$Z = \frac{2-n}{2} k \left(\sigma_{t,\max} b \sqrt{\pi}\right)^n a_0^{\frac{2}{2-n}} \tag{20}$$

2.2.4. Resistance increase

The film ionic conductivity k_{SEI} and thickness of the SEI layer δ_{SEI} both have an impact on its resistance. The lithium plating, on the other hand, does not affect ionic conductivity, hence the resistance increase is governed solely by the SEI layer, implying that the SEI film resistance can be found as:

$$R_{SEI} = \lambda_{SEI} \frac{\Delta\delta_{film}}{k_{SEI}} + \frac{\delta_{film,0}}{k_{SEI}} \tag{21}$$

where λ_{SEI} is the volume fraction of SEI layer in the deposited film, δ_{film} is defined as the ratio of the total volume to the specific surface area A_v, in which equivalent thickness of lithium plating contributes to the total film thickness, i.e.

$$\Delta\delta_{film} = \frac{1}{3600 A_v} \left(\frac{\lambda_{SEI} Q_{SEI} M_{SEI}^{inorganic}}{2\rho_{SEI}^{inorganic} F} + \frac{(1-\lambda_{SEI}) Q_{SEI} M_{SEI}^{organic}}{2\rho_{SEI}^{organic} F} + \frac{Q_{Li} M_{Li}}{2\rho_{Li} F}\right) \tag{22}$$

where α is the volume fraction of the inner inorganic SEI layer.

The interfacial dynamics are affected by the low discharge rate, resulting in a low overpotential at the anode interface. The Butler-Volmer equation indicates that the equivalent R_{CT} can be determined as:

$$R_{CT} = \frac{1}{L_{neg} A_v} \frac{RT}{j_{tot}(\alpha_a + \alpha_c) F} \tag{23}$$

SEI film growth and lithium plating lead to a reduction in anode porosity, and accelerate the thickness of the film and the drop of porosity, which is modeled by relating the change in anode porosity to the increase in surface film thickness:

$$\varepsilon_n(N) = \varepsilon_{n,0} - A_v\left(\delta_{film}(N) - \delta_{film,0}\right) \tag{24}$$

where δ_{film} is the total equivalent thickness of deposited surface film, ε_n is the porosity of anode, and N indicates the aging cycles.

The established electrochemical-mechanical coupled model based on Eqs. (1)–(24) are used to get a digital twin of NMC LiBs cycling at room temperature with 1C, 2C and multi-step constant current (MCC). All the parameters related to electrodes and electrolyte are summarized in Table S-1. Aging parameters related to SEI growth, lithium plating, and mechanical cracking are summarized in Table S-2. The next chapter provides details on material property parameters, including SOC intervals for active materials and OCV of electrodes determined by coin cell tests. Temperature-related properties are taken from the COMSOL Multiphysics 6.1 materials database.

3. Experiment

3.1.1. Dynamic aging conditions

In this work, commercially available 18650 cylindrical NMC Samsung battery cells (Φ18.33 × 64.85 mm, capacity 2 Ah, nominal voltage 3.6 V, maximum charge current 4 A) were used. The cathode and anode materials are $LiNi_{0.5}Co_{0.2}Mn_{0.3}O_2$ and synthetic graphite, respectively. Before proceeding with aging testing, a preconditioning test at 1C constant current constant voltage (CC-CV) charging and discharging was carried out to verify the thermodynamic stability of the cells and to ensure that outlier samples are identified. Three cycle aging test cases were designed and performed at 25 °C, with one battery in each test case. The test flowchart, consisting of the precondition test, dynamic aging test, performance test, and post-mortem analysis, is shown in Fig. 3. The dynamic aging test and the performance test were repeated until the cells reached 10 % capacity fade. The test instruments, including an operando EIS tester, aging tester, temperature chambers, and an online monitoring PC are illustrated in Fig. 3. Additionally, objectives of this study are full cells and fresh coin cells.

3.1.2. Dynamic aging test program

For the first two aging cases, the cells were initially charged to 4.2 V using CC-CV profiles with different C-rates of 1C and 2C, respectively. When the current fell to 0.1 A, the cells were considered fully charged. For the last case, multi-step constant current constant voltage (MCCCV) charging was developed to compare the influence of the charging process on the cycle life of LiBs. A detailed description of the three aging cases can be found in [27]. All cells were discharged using the World Harmonized Light Vehicles Test Cycle (WLTC) profile.

A reference performance test (RPT) was performed, at 25 °C, after every 100 full equivalent cycles (FECs) to investigate and quantify the incremental degradation of the capacity of the cells. The cells were charged to 4.2 V using a CCCV profile with a current of 0.5 C (i.e., 1 A); when the cut-off current reached a value of 0.1 A, the cells were considered fully charged. Then, the cells were fully discharged to 2.5 V by a constant current of 0.5 C (i.e., 1A). The capacity measured during discharging is used in the upcoming analysis to quantify and model the capacity fade behaviour of the cells during aging.

Operando EIS test was conducted using Digatron analyzer within the frequency range of 6.5 kHz to 10mHz at 80 % SOC. The impedance spectra measured on the three cells throughout the aging tests (see Fig. 4(a) - Fig. 4(c)) were fitted using the equivalent circuit model (ECM) (see Fig. 4(f)) provided in the ZfitGUI software. The resistance increase associated to the SEI layer and charge transfer process are plotted in Fig. 4, respectively. Discussions of these results and a detailed comparison with physics model results are given in Section 4.2.

3.1.3. Coin cell measurements

Coin cell tests were performed to measure the OCV curve for the NMC and graphite electrodes, as well as the stoichiometry at 0% and 100%. The NMC cathode and graphite anode were cut from freshly dismantled 18650 cylindrical batteries, then paired with a 15 mm diameter lithium metal disc. A 1:1 mixture of ethylene carbonate (EC) and diethyl carbonate (DEC) with 1 M LiPF6 served as the electrolyte.

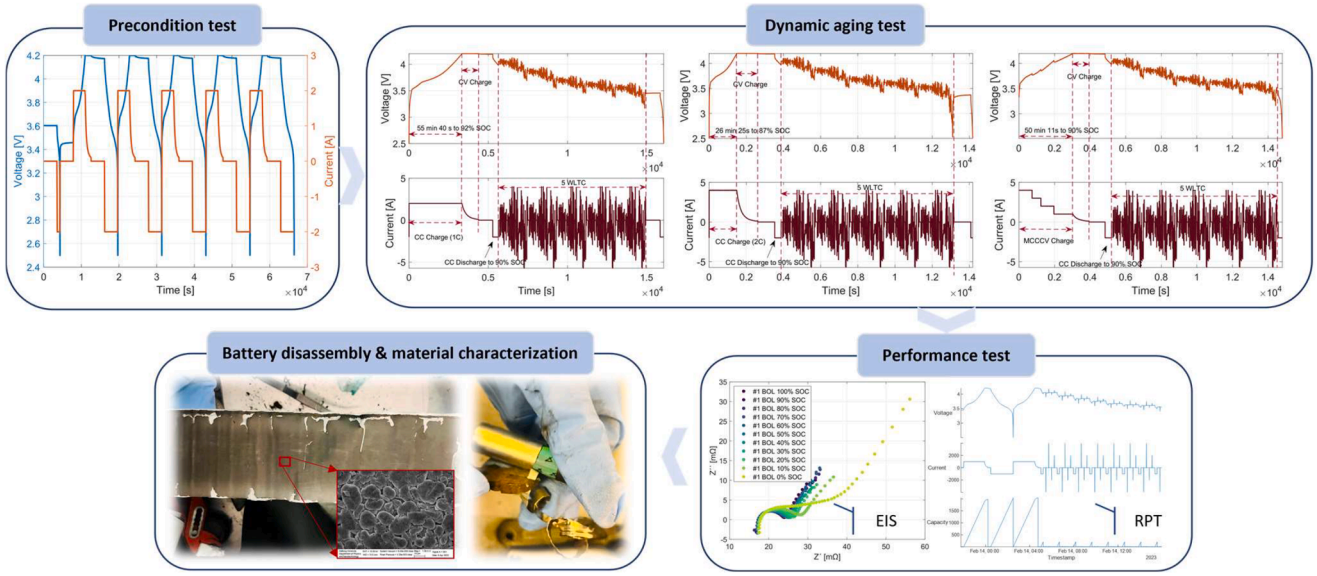

Fig. 3. Overview test flowchart including precondition test, dynamic aging test, performance test, and post-mortem analysis.

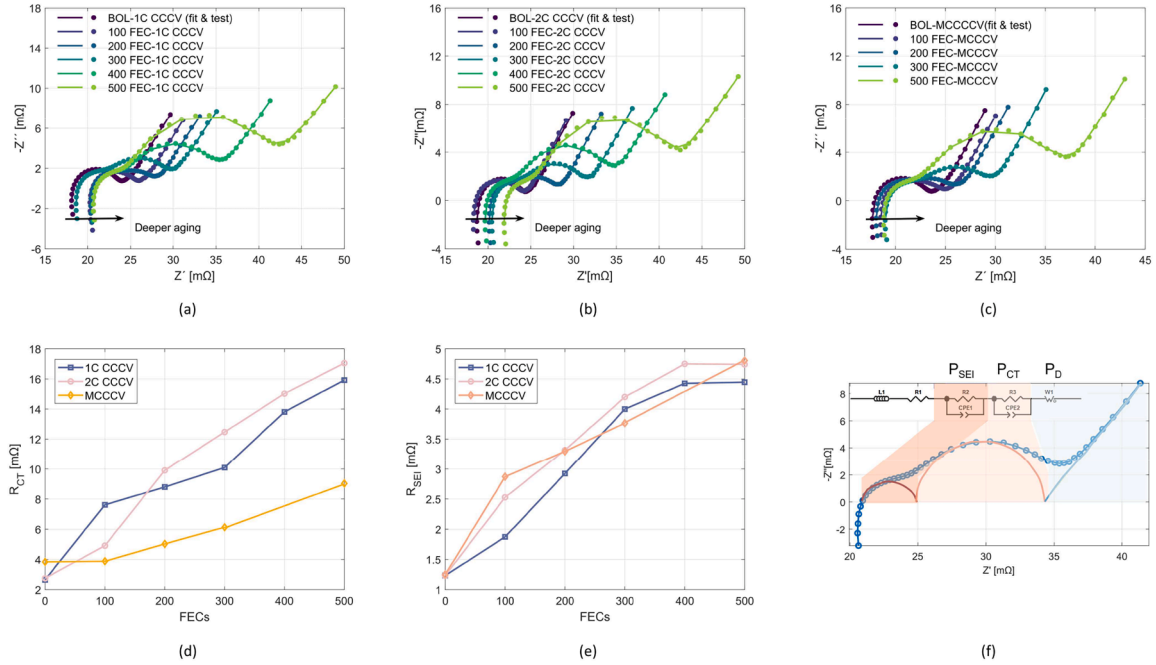

Fig. 4. EIS test and ECM fitting curve. EIS results and fitting curve for (a) 1C CCCV, (b) 2C CCCV, and (c) MCCCV at 80% SOC, (d)R_{SEI}, and (e) R_{CT} for three charging protocols, (f) ECM model illustration, note that P_{SEI} represents the physical source of SEI diffusion, while P_{CT} is associated with the charge transfer of lithium ions at the interface, and P_D denotes the diffusion of lithium ions within the anode/cathode particles.

Graphite/Li and NMC/Li coin cells were charged and discharged with a Landt coin cell tester at a constant current of 0.8 mA, corresponding to a 0.2 C-rate. The OCV test results are shown in Fig. 5.

3.1.4. Material characterization

A Scanning Electron Microscope (SEM, Zeiss XB1540, Carl Zeiss) operating at 20 keV was used to characterize the morphology of the anode electrode surface after the aged cells reached 10 % capacity loss. The cells with 500 FECs aging were fully discharged, moved to a glove box filled with argon gas and disassembled to validate the model's quantitative characterization results for SEI growth and graphite crack propagation. Following that, the electrodes were thoroughly washed three times with DEC and immediately transferred for further characterization. Detailed findings will be shown in Section 4.

4. Results and discussion

4.1. Model validation

The cell voltage was found to have a significant impact on seven capacity-related parameters [35], namely $C_{s,max}$, L_p, L_n, ε_n, ε_p, r_n, and r_p. Upon conducting an in-depth analysis of these sensitive parameters using the Morris One-At-a-Time (MOAT) method, it has been determined that the influence of r_n and r_p on the capacity results is negligible (detailed results can be found in Fig. S2). The particle radius parameter is determined experimentally using SEM (see Fig. 7(a) and (c)) to gauge

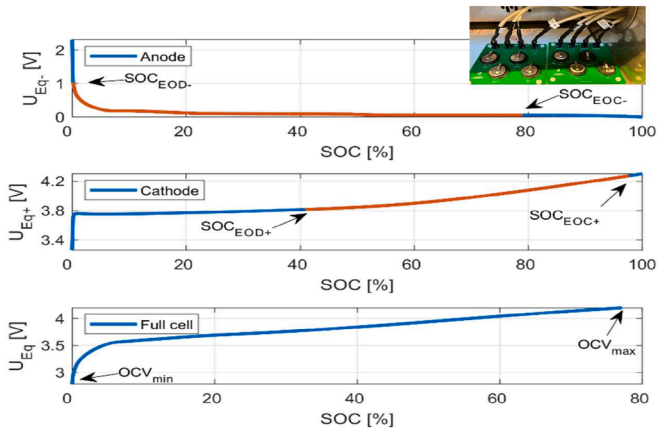

Fig. 5. OCV – SOC curves with the end of discharge (EOD) and end of charge (EOC) of the fresh two electrodes and full cell obtained throughout coin cell measurements.

the particle size distribution as shown in Fig. 7(b) and (d). This demonstrates that the particle size follows a normal distribution within a certain range. The model utilizes the mean value, considering the minor MOAT effect. The remaining five parameters were optimized using the voltage and current data recorded at the fresh state with the CCCV protocol based on already integrated P2D models in COMSOL. Fig. 6(a) and(b) depict the optimized current and voltage profiles obtained from 1C and 2C CCCV charging protocols. The mean absolute errors (MAEs) for current and voltage at 1C are 3.15 and 2.47 %, while at 2C they are 4.08 and 3.84 % respectively.

Fig. 8(a) illustrates the capacity degradation measured from RPTs for the three aging conditions during cycling. Numerical simulation results based on established physics models and experiment data are found to agree well. The results reveal that the capacity of CCCV charging protocols decreases almost linearly in the early cycles, from 2.04 Ah and 2.03 Ah at the beginning to 1.81 Ah and 1.79 Ah at the 200th FEC (about 43.23 mAh loss for 1C rate and 44.20 mAh loss for 2C rate per cycle). After that, the cells age faster and drop to 1.81 Ah and 1.79 Ah after 500 FECs (about 51.33 mAh loss for 1C rate and 51.90 mAh loss for 2C rate per cycle). When compared to the CCCV protocol, MCCCV has a greater rate of degradation for the first 200 FECs (around 48.53 mA loss per cycle), and then ages with 27 mAh loss per cycle to 1.82Ah at the 500th FEC. The degradation trajectory shows an exponential asymptotic trend.

Fig. 8 (b) depicts the battery energy degradation over time. The battery's energy is estimated by integrating the charging power during charging time and calibrated by the total charging energy during RPT. In its fresh state, the battery delivered 7.46, 7.45, and 7.41 Wh under the three aging conditions. After aging (500 FECs), the battery's energy output significantly decreased, providing only 6.31 Wh at 2C CCCV, which had the fastest energy degradation of 14.82 %, followed by 6.36 Wh at 1C CCCV (15.24 % loss), and the MCCCV protocol with a maximum of 6.55 Wh and an 11.55 % fade. The figure demonstrates that our model successfully captures the energy degradation, depicting the initial energy fluctuations [36], as well as a sustained energy drop at a later stage.

To better validate the reasonability of the physics model, charge voltage curves at each 100 FECs in different aging conditions are compared, as shown in Fig. 9. The model results match well with the experiment data, most of the time with RMSE and MAE below 4 %. The advance of the moment when the charging voltage reaches 4.2 V indicates the irreversible capacity fade with aging. Real-time voltage and current can be captured and predicted by digital twin shown in Fig. S2.

4.2. SEI growth effect

The SEI layer model, which considers the impact of capacity fade on solid phase concentration as given by Eqs. (4) and (6) and the influence of SEI layer growth on resistance as given by Eq. (21), results in a change in the solid phase volume fraction of the active material. Fig. 10 illustrates the measured capacity fade for the three cases and the simulated capacity fade considering only models in Section 2.2.1. The considered models exhibit a minimal variation of capacity fade between the three aging cases, estimated to be only 0.03 % after 200 full equivalent cycles (FECs). However, this variation increases to 0.3 % after 500 FECs. Although the model initially matches well with the measured capacity fade during the first 200 FECs, it deviates significantly up to 3.9 % after 500 FECs. Fig. 11 shows that after 500 FECs, SEI films were observed on the anode surface under all three protocols using SEM. The results obtained through simulations suggest that the capacity fade caused by SEI growth will stabilize into a linear variation. However, the measured capacity results indicate that in addition to the SEI growth mechanism, other mechanisms are at play that results in a non-linear rollover effect.

The relationship between the predicted relative increase of SEI film resistance and the experimental results obtained by fitting the ECM to impedance spectra measured at 80 % SOC is depicted in

Fig. 12(a-c). The MAEs for relative R_{SEI} (%) at 1C CCCV, 2C CCCV, and MCCCV are 7.69, 10.18 and 4.78 %, respectively. They indicate that higher C-rates lead to faster SEI growth, i.e., the battery aged by charging the battery with 2C-rate has the fastest growth rate of R_{SEI}, resulting in a thicker SEI film and subsequent capacity fade. Furthermore, the resistance of SEI film grows more significantly in the separator-side area, leading to a local decrease in porosity [10,37]; this decrease in porosity is illustrated in

Fig. 12(e) which shows the distribution of local anode porosity for a

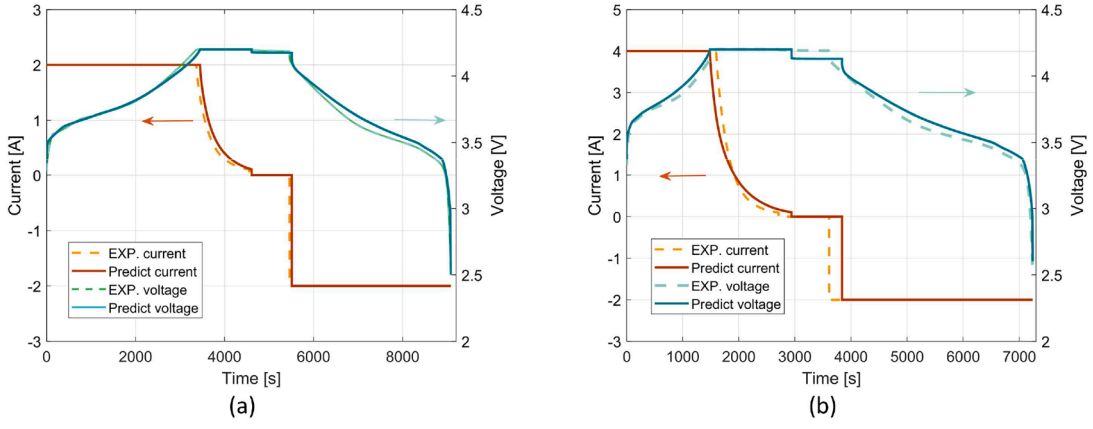

Fig. 6. Optimized current and voltage response to calibrate the physics model for CCCV protocol using (a) 1C and (b) 2C charging protocols.

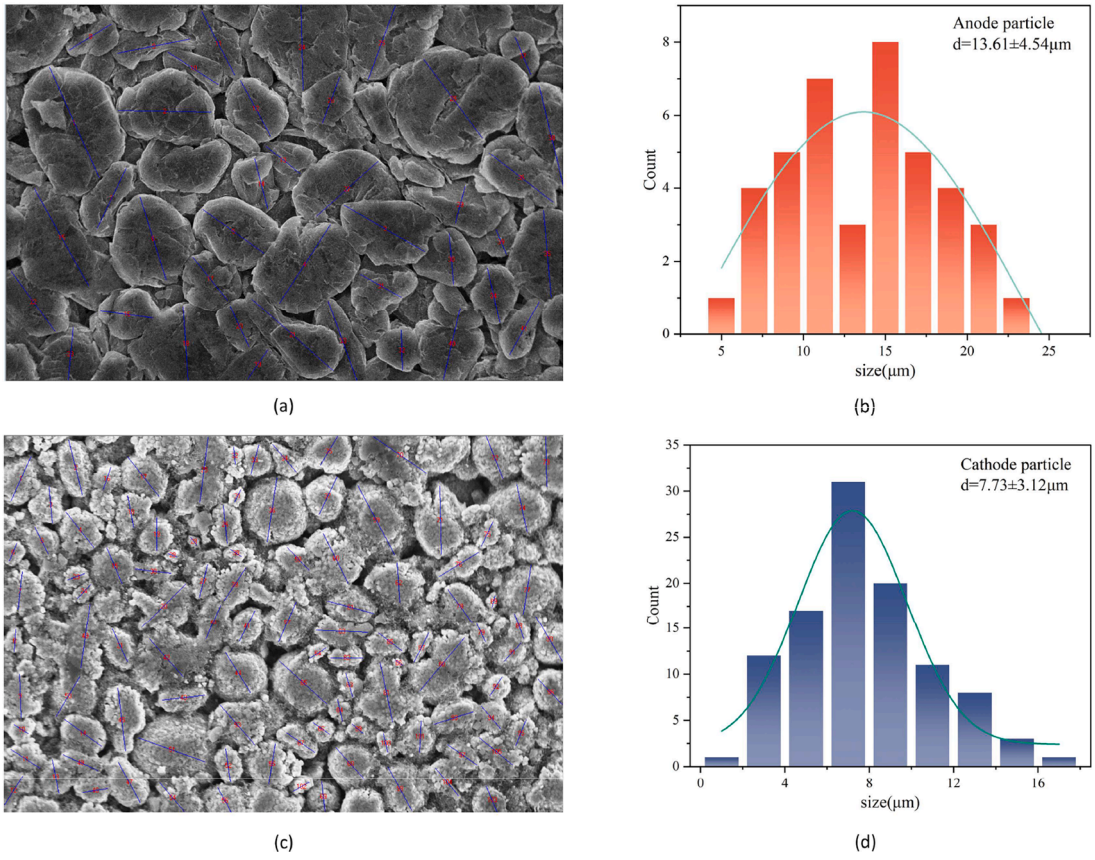

Fig. 7. Parameter identification (a, c) SEM images for anode and cathode particles, (b, d) Mean value of Normal distribution for particle radius.

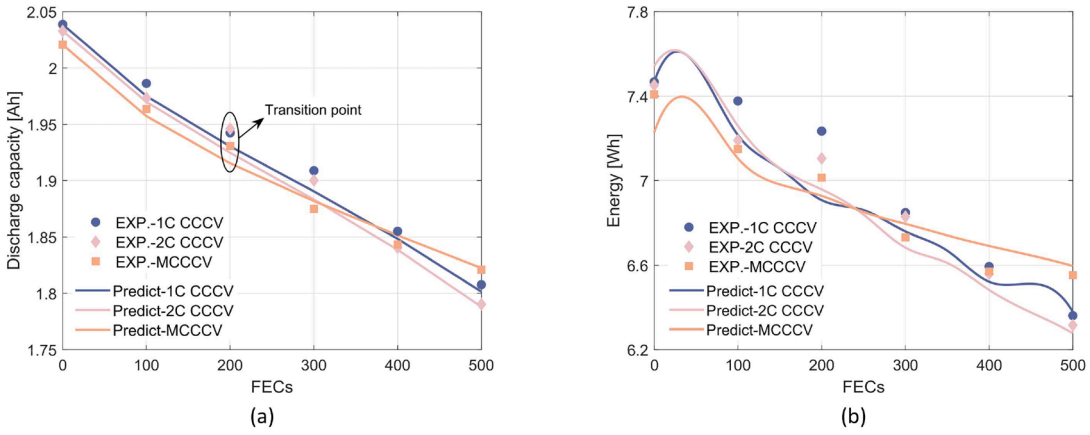

Fig. 8. Comparison of experimental and predicted (a) capacity and (b) energy degradation in three aging conditions.

fresh cell and the aged cells after 500 FECs. It is evident that the total current density at the anode decreases continuously with aging, and the anode porosity also decreases with aging (

Fig. 12(e)). The porosity of the fresh cell is 0.67, and after 500 FECs, 2C CCCV causes the most significant decrease in porosity near the anode/separator interface, dropping below 0.56, followed by 1C CCCV (below 0.58). MCCCV exhibits almost the same pore clogging on the current collector side as 1C CCCV, but the separator side pore clogging is better than 1C CCCV. The measured resistance increase of the charge transfer, R_{CT}, for the cells aged under the three charging protocols are illustrated in

Fig. 12(d) together with the estimated values, which were computed based on Eq. (23). The MAEs for relative R_{CT} (%) at 1C CCCV, 2C CCCV, and MCCCV are 5.11, 2.73 and 3.59 %, respectively. The finding demonstrates that the R_{CT} of 2C CCCV aged cells shows the highest increase, followed by cells aged under 1C CCCV and MCCCV protocols. The charge transfer process is influenced by factors such as electrode thickness, particle size of the active material, and interface side reactions [38]. As the cells used in this study were sourced from the same batch, it is reasonable to assume that they possess uniform thickness and active material properties. Consequently, the results indicate that the side reactions during the aging process under 2C CCCV protocol are particularly prominent, thereby exerting an influence on the reaction of lithium ions and electrons combining and delithiating at the anode interface. In addition, the difference in the decrease of capacity density caused by SEI growth is less than 0.2 Ah/m^2 between the three charging

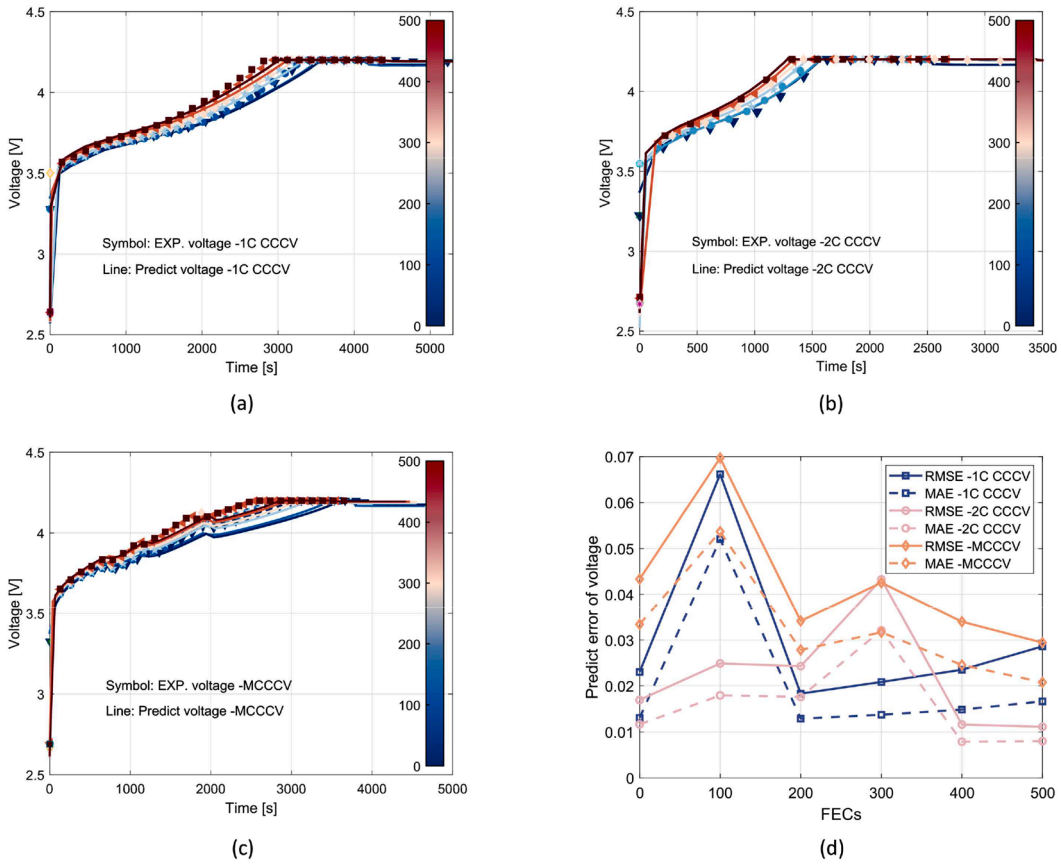

Fig. 9. (a-c) Comparison of model results with test data in terms of charging voltage with FECs during cycling aging, (d) predict voltage error in the three charging protocols.

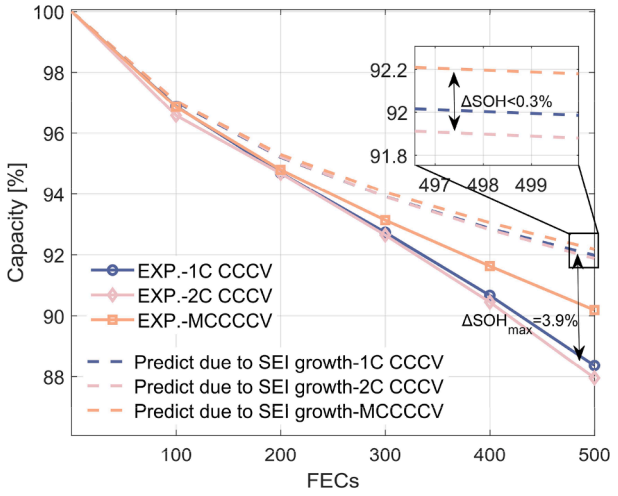

Fig. 10. Comparison between the measured capacity fade and estimated capacity fade when considering only the SEI growth as battery aging mechanism.

protocols, with 2C CCCV being slightly greater than 1C CCCV, while MCCCV being the smallest after 500 FECs. This suggests that aging a battery with a high current at room temperature does accelerate the SEI formation to some extent but is not a key factor in the rapid growth of SEI film. This behaviour is well aligned with the results presented in [39].

4.3. Crack formation effect

The electrochemical potential difference serves as the driving force for the diffusion of lithium ions, resulting in the formation of a concentration gradient within a graphite particle. This diffusion-induced concentration gradient leads to the expansion and contraction of the particle, resulting in stress generation. A spherical isotropic diffusion-induced stress model was employed to determine the stress generation as lithium ions diffuse radially within the particle. The peak along the tangential and axial tensile stresses for all three charging strategies occurs at the centre of the particle during the onset of lithiation during charging (as shown by solid lines in Fig. 13). The maximum tangential and axial stresses corresponding to both 1C and 2C charging strategies are observed at the end of the CC charging section, with the stresses at 2C being approximately twice as large as those at 1C. For the MCCCV charging strategy, the maximum tangential and axial tensile stresses occur at 80 % SOC, when the charging current switch from 1 C to 0.5 C. Numerical solutions obtained using COMSOL indicate that the tangential and axial stresses exhibit opposite signs during lithiation and delithiation, as depicted by the dashed lines representing the end of discharge (EOD) in Fig. 13. This accumulation of tangential stresses at the crack opening over multiple cycling times is a driving factor for fatigue crack nucleation, which ultimately leads to the formation of microcracks on the particle surface after cycling.

For better visualization, an ideal sphere model is used to represent the anode particles, with a quarter of the particle omitted. The lithium-ion concentration and corresponding tangential stress at EOD are plotted. The results reveal that the anode particles exhibit the largest concentration at the centre of the delithiation state, with the largest concentration gradient observed in the 2C CCCV condition, along with a correspondingly larger surface-to-centre tangential stress gradient (i.e.,

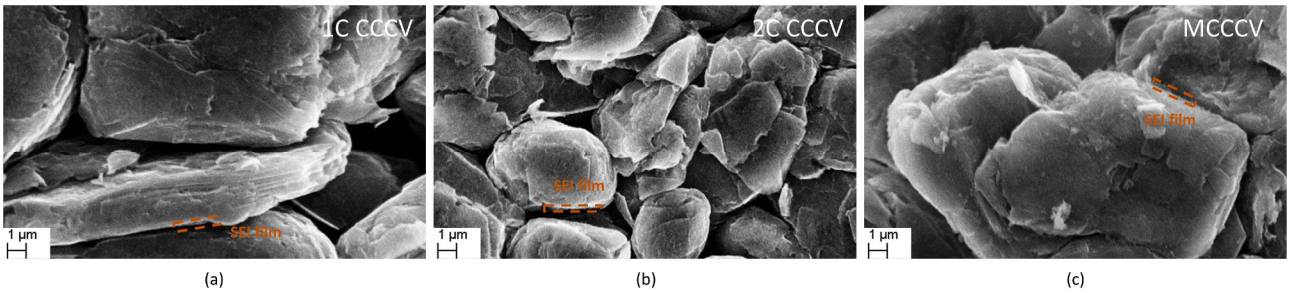

Fig. 11. SEM images highlighting the SEI film after the three cells reached 10% capacity fade.

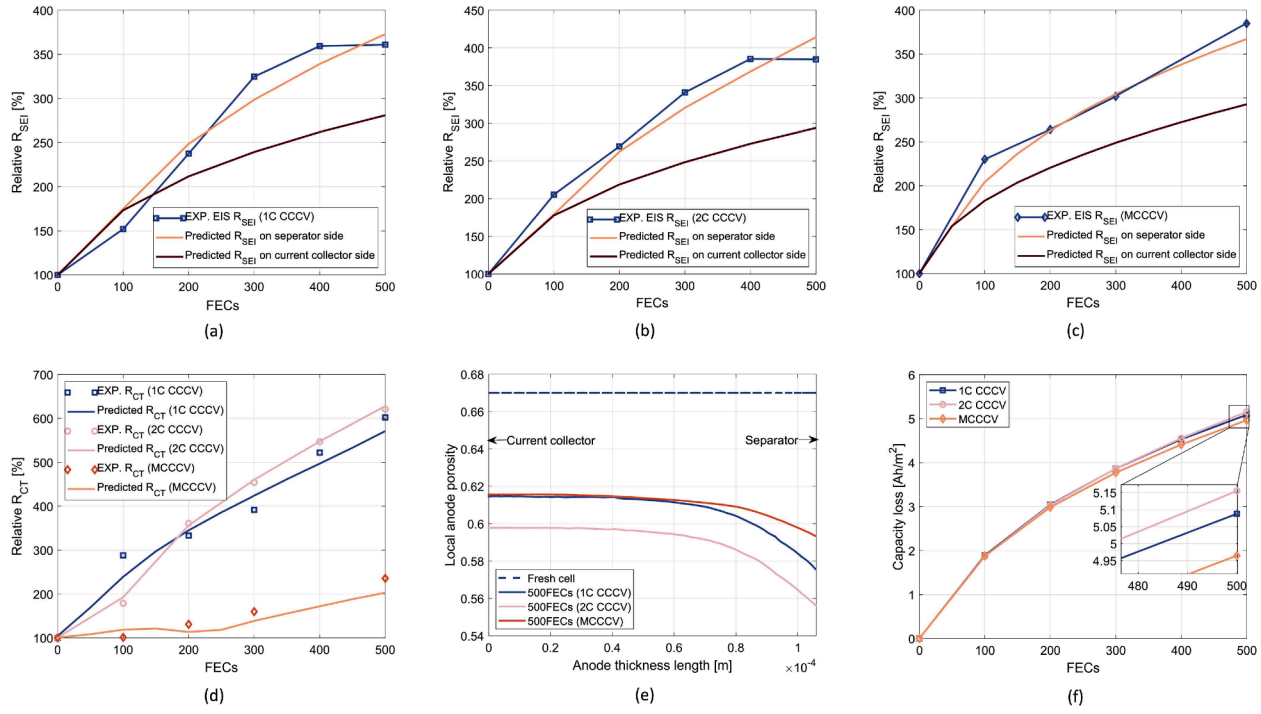

Fig. 12. Comparison of the experimental and predicted SEI film resistance and SEI film at theanode/separator and anode/current collector sides for (a) 1C CCCV, (b) 2C CCCV, (c) MCCCCV, (d) comparison of the experimental and predicted charge transfer resistance increase for three charging protocols, (e) local anode porosityfor a fresh cell and after 500 FECs and (f) decrease of capacity density for the three protocols due to SEI film growth.

$\sim 2 \times 10^7$ Pa). The 1C CCCV condition shows a slightly smaller particle concentration gradient compared to 2C CCCV, with a tangential stress level similar to the 2C CCCV (i.e., $\sim 1.8 \times 10^7$ Pa). On the other hand, the MCCCV condition exhibits the smallest lithium-ion concentration gradient and corresponds to a smaller intercalation tangential stress compared to CCCV protocols ($\sim 1.2 \times 10^7$ Pa). Furthermore, our results show that the stress peak induced by lithium-ion diffusion is highest during the CC-CV charging above 80% SOC, independent of the battery being charged with1C or 2C. Conversely, for MCCCV charging, the stress peak is highest during the third CC switching current amplitude which happens at 80 % SOC, this behaviour is consistent with our prior observations [27]. These findings imply that utilizing low current charging above 80 % SOC can alleviate anode stress peak and reduce anode crack formation.

The effect of crack propagation for the three aging conditions is quantified using the ratio of $\Delta a/a_0$, which represents the change in crack depth related to the initial crack depth and is depicted in Fig. 14(a). The evolution of crack depth is observed to occur in three distinct phases. Initially, the crack depth increases slowly, followed by an accelerated stage where the growth rate of the fatigue crack significantly increases. Finally, the cracks undergo a fast growth stage resulting in significant particle cracking. The growth of crack plays a critical role in triggering capacity fade, with the accelerated and rapid growth phases showing a non-linear degradation in capacity at a macroscopic level. Lower C-rates lead to smaller lithium-ion concentrations and thus reduce stress levels Eq. (10)), which in turn slows down crack growth (Eq. ((11)) and extends the overall life of the cell. Experimental evidence has indicated that stresses can accumulate within anode particles [15], although monitoring stress at the particle level through in situ measurements remains challenging. Nevertheless, the crack extension rates predicted in this study fall within the range of values reported in [16].

4.4. Lithium plating effect

The negative electrode potential (NEP) at the anode/separator interface and SOC of the cell, initially and after 500 FECs, are plotted based on Eqs. (7) and (8) for three charging protocols. The results indicate that the length of time for lithium plating increases with aging time for CCCV protocol. Moreover, the MCCCV charging protocol exhibits significantly less lithium plating than the CCCV. In all three conditions, SOC at the onset of charging increases with aging time, the end of the CC stage decreases, and the CV phase becomes progressively

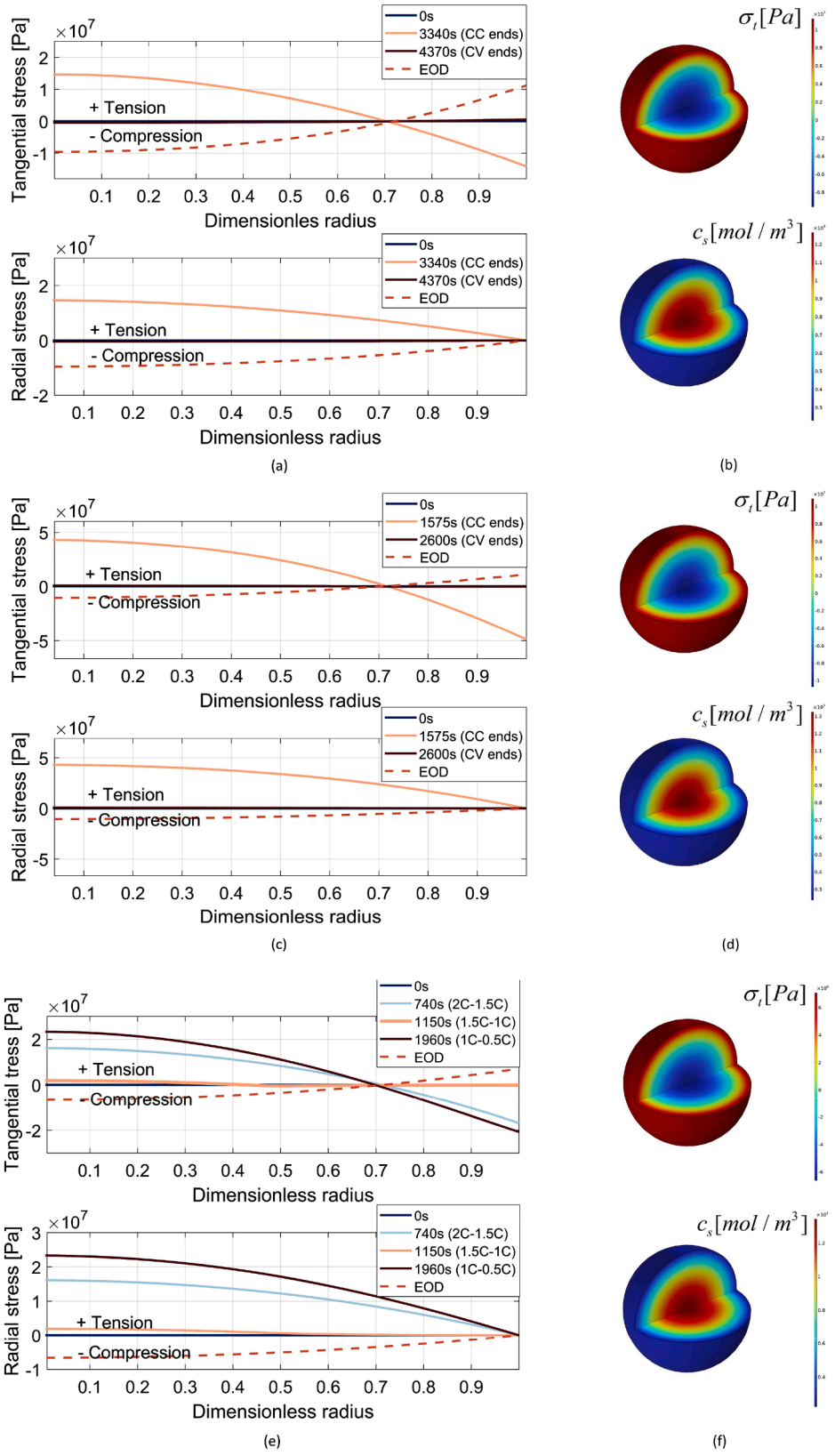

Fig. 13. Mechanical analysis for the anode electrode. Tangential (top subplot) and radial (bottom subplot) stress distribution inside anode particle at the end of CC stage, CV stage and at the EOD for (a)1C CCCV-WLTC aging case, (c) 2C CCCV-WLTC aging case, and. (e) MCCCV-WLTC aging case. (b, d, and f) Corresponding Li+ concentration gradient and tangential stress at the EOD stage for three aging protocols.

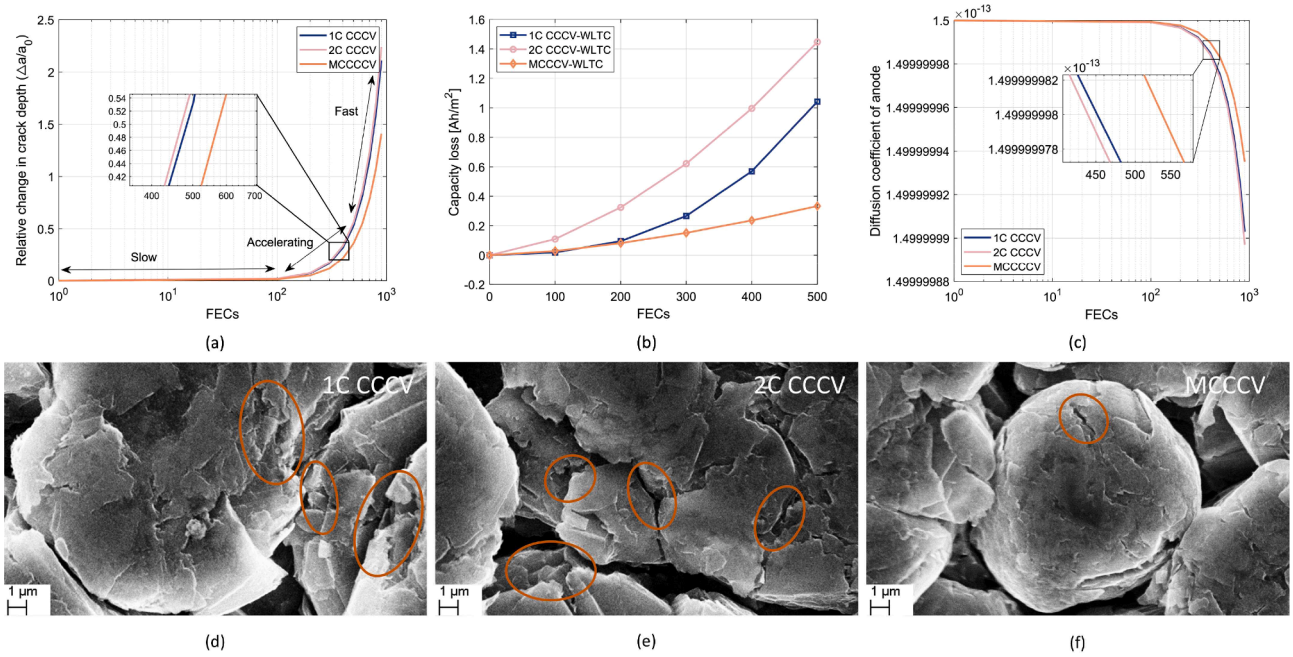

Fig. 14. Crack propagation versus aging cycles (b) Capacity fade due to crack propagation, (c) diffusion coefficient of the anode at three aging conditions, and (d-f) SEM morphology characterization of three aging conditions.

longer. More detailly, when charging using the 1C CCCV protocol, the NEP on the separator side drops below 0 V at 3300 s, for the fresh cell. However, for an aged cell (i.e., after 500 FECs), the NEP drops below 0V at 2260s, and a minimum potential of -0.05 V indicates pronounced lithium plating. When charging using the 2C CCCV protocol, the NEP drops below 0 V after 1200 s, for the fresh cell, reaching a lower potential of -0.06 V compared to 1C CCCV case, resulting in faster initial lithium plating. After aging at 500 FECs, the NEP dropped below 0 V after only 655 s, with a minimum potential of -0.11 V. The MCCCV protocol, when compared to the CCCV protocol, led to a slower activation condition for lithium plating, resulting in minimum lithium plating. Interesting is the fact that, for a fresh cell, as the SOC ranges from 80 % to 100 %, the anode potential remains above 0 V until the charging C-rate reaches 0.5 C. However, upon reaching the cut-off voltage of 4.2 V, the voltage drops to -0.02 V, subsequently followed by a short CV period. Remarkably, during this CV period, the NEP swiftly restores to 0 V. It should be noted that the plating reaction tends to move from the separator electrode interface to the current collector, with the interface on the separator side being the first to start plating lithium, resulting in more prominent lithium plating at the separator interface. Moreover, with all three charging protocols, the NEP initially drops below 0 V at the current collector interface, and almost no lithium plating appears after 500 FECs.

Considering that lithium plating occurs mainly on the anode separator side (Fig. 15), the local volume current density at the anode separator interface is plotted in Fig. 16. The model in this study assumes that no lithium plating occurs at BOL, so here the reaction current densities are compared between 100 FECs and 500 FECs to illustrate the changes in the internal reactions during aging. At 100 FECs (dashed line), the charging starts with a regular intercalation for both 1C CCCV and 2C CCCV. The intercalation current density is higher for 2C CCCV, approximately twice as high as 1C CCV, until the anode potential drops below 0 V. This drop occurs at approximately 78 % SOC for 1C CCCV and 56 % SOC for 2C CCCV, initiating lithium plating. The plating reaction occurs after the intercalation current density has reached its maximum. When switching to the CV stage, the volumetric current density for lithium plating reaches a maximum (at approx. 92 % SOC and 81 % SOC for 1C CCCV and 2C CCCV, respectively) and then begins to decrease due to an increase in the plating overpotential and a simultaneous decrease in the charging current. At 100 % SOC, after the anode potential exceeds 0V, the volumetric current density of the plating drops to zero and the lithium plating stops. At 100 FECs, the intercalation current of the MCCCV-aged cell is smaller than that of the 2C CCCV-aged cell but larger than that of the 1C CCCV-aged cell. Lithium plating starts around 95 % SOC, peaks at the beginning of the CV section (98 % SOC), and stops at 100 % SOC when the CV phase concludes, resulting in a plating

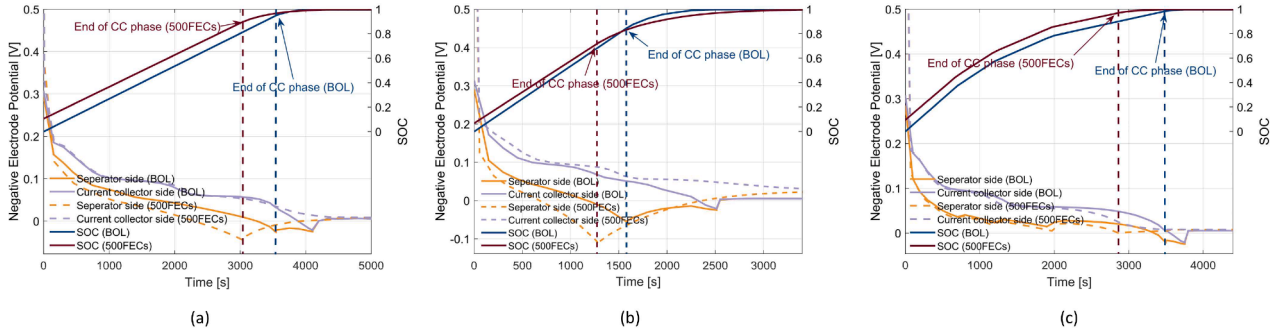

Fig. 15. Battery SOC during the charging phase at BOL and after 500FECs and LDP at the separator interface and the current collector interface for three aging strategies (a) 1C CCCV, (b) 2C CCCV, and (c)MCCCV

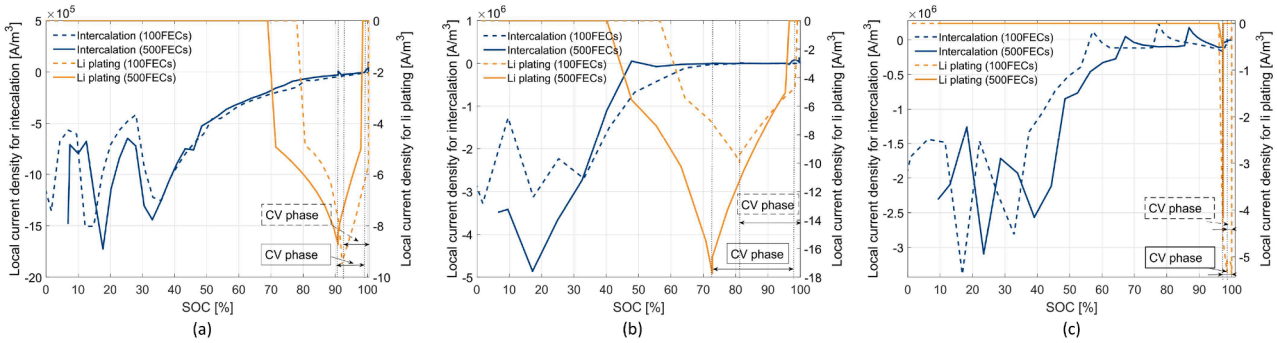

Fig. 16. Intercalation and lithium plating current density at the anode/separator interface for three charging protocols, (a) 1C CCCV, (b) 2C CCCV, and (c) MCCCV during CCCV charging at 100FECs and 500FECs.

current density of 0. This significantly reduces the duration of time that the anode is subjected to lithium plating. After 500 FECs, the intercalation current onset shifts towards lower SOC for all three aging protocols, indicating that aging affects the battery's charge and discharge capacity, and the battery cannot fully return to the initial 0 % SOC. Specifically, for the cells aged under the 1C CCCV and 2C CCCV protocols, the intercalation response shifts from 0 % SOC to 6 % SOC, while for the cell aged under the MCCCV protocol, the intercalation response only begins at approximately 10 % SOC at 500 FECs, which is particularly noteworthy. Moreover, during aging, both 1C and 2C aging protocols lead to an increase in the duration of time when the anode is subjected to lithium plating, until the anode potential drops below 0 V at 500 FECs (at around 69 % SOC and 40 % SOC for 1C CCCV and 2C CCCV, respectively), triggering the onset of lithium plating. During the CV stage, the volumetric current density for lithium plating reaches a maximum (at approximately 90 % SOC and 73 % SOC) and then starts to decrease. Interestingly, for the MCCCV protocol, after 500 FECs, lithium plating occurs from 95 % SOC, with the maximum lithium plating current density observed at 97 % SOC, followed by a rapid drop to 0, indicating a reduction in lithium plating time compared to 100 FECs.

The models based on Eq. (8) can predict the capacity loss of plated lithium, which increases with the charging current, as depicted in Fig. 17. The capacity loss due to lithium plating is 0.071 Ah/m^2, 0.023 Ah/m^2, and 0.012 Ah/m^2 for a charging current of 2C, 1C, and MCC, respectively. These values correspond to 0.13, 0.041 and 0.022 % of the rated cell capacity of 2 Ah. The impact of lithium plating on the capacity degradation at 25 °C for three protocols is negligible compared to the impact caused by SEI growth and cracking, with a difference of two orders of magnitude. And again, we are not able to capture the lithium dendritic phenomenon using SEM. This indicates that lithium plating has no significant effect on the initial 10% capacity loss, even under high current conditions. This finding is in line with the observations reported by [10] regarding the lithium plating phenomenon occurring below 0°C. However, the potential for lithium plating to increase exponentially under high C rates, such as 2C, may lead to non-linear rapid degradation in the future, as observed in the capacity rollover triggered by fast charging currents of 1C and above, as reported by [8].

5. Conclusions

This paper introduces an advanced digital twin to capture real-time data for quantitatively analysing the SEI growth, crack propagation, and lithium plating coupling mechanisms in NMC-based LiBs using dynamic aging profiles, which has important implications for battery aging behavior prediction, mechanisms quantification, and charging protocol development in real-world applications. The model is calibrated through iterative optimization of real-time voltage and current behavior to identify the most sensitive parameters. Subsequently, the calibrated model is employed to unravel aging mechanisms' effects under three charging protocols with dynamic discharging profiles. SEI growth is found to be the primary contributor to degradation, and although SEI-induced degradation is minimal under the MCCCV protocol, the SEI-induced SOH degradation for 1C CCCV, 2C CCCV, and MCCCV differs by less than 0.3 %. This was verified by the SEI resistance growth obtained from the operando EIS measurements. Cracking provides a non-linear accelerated aging driver after 200 FECs, with crack propagation at an almost stable stage during the first 200 FECs, after which accelerated crack growth induces SOH decrease. The growth of anode cracks under the MCCCV aging protocol has a much slower effect on degradation behavior compared to the 1C CCCV and 2C CCCV, as strongly confirmed by the post-mortem analysis. The lithium plating phenomenon triggers two orders of magnitude less capacity degradation than SEI growth and cracking. Although high current charging causes the overpotential to drop below 0 V, the reaction current density of the lithium

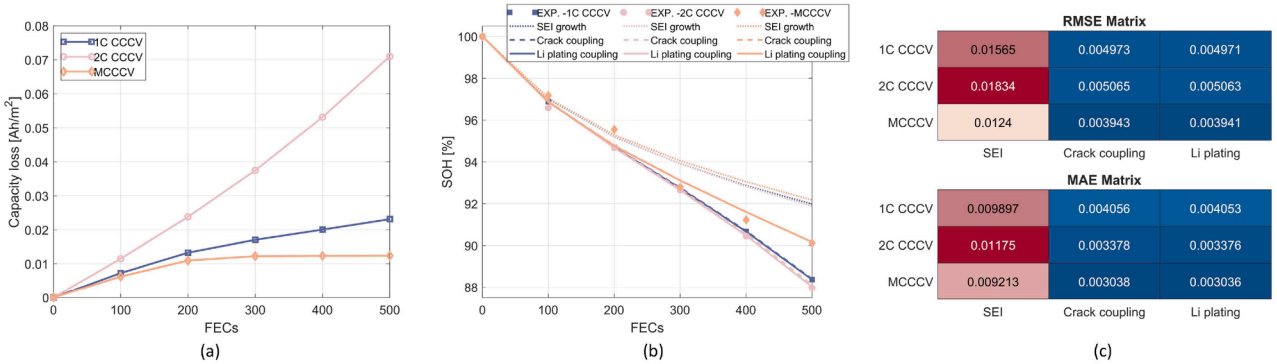

Fig. 17. (a) Capacity loss due to lithium plating, (b)comparison of predicted and experimental SOH considering three mechanisms coupled, and (c) digital twin errors.

plating is five orders of magnitude less than the main intercalation reaction and has a negligible effect on the NMC battery performance. Furthermore, the proposed MCCCV charging protocol can charge the battery from 0 % SOC to 90 % SOC in approximately 50 min and reduce degradation effects. The digital twin can predict voltage profile within 4 % MAE and battery SOH degradation within 0.4 % MAE. It will be combined with machine learning to develop a physics-informed machine learning model for predicting battery aging behavior in the future.

CRediT authorship contribution statement

Wendi Guo: Conceptualization, Investigation, Methodology, Writing – original draft, Visualization, Validation, Funding acquisition, Project administration. **Yaqi Li:** Writing – review & editing, Validation, Funding acquisition. **Zhongchao Sun:** Investigation, Methodology, Writing – review & editing, Validation, Funding acquisition. **Søren Byg Vilsen:** Writing – review & editing, Supervision, Project administration. **Daniel Ioan Stroe:** Conceptualization, Writing – review & editing, Supervision, Project administration.

Declaration of Competing Interest

The authors declare that they have no known competing financial interests or personal relationships that could have appeared to influence the work reported in this paper

Data availability

The authors do not have permission to share data.

Acknowledgments

This work has been funded by China Scholarship Council. The fund numbers are 202006220024, 202106020069 and 202106020070.

Supplementary materials

Supplementary material associated with this article can be found, in the online version, at doi:10.1016/j.ensm.2023.102965.

References

[1] C. Pillot, The rechargeable battery market and main trends 2020-2030, Batter. Event 2021. (2021).
[2] C.R. Birkl, M.R. Roberts, E. McTurk, P.G. Bruce, D.A. Howey, Degradation diagnostics for lithium ion cells, J. Power Sources 341 (2017) 373–386, https://doi.org/10.1016/j.jpowsour.2016.12.011.
[3] J. Guo, S. Jin, X. Sui, X. Huang, Y. Xu, Y. Li, P.K. Kristensen, D. Wang, K. Pedersen, L. Gurevich, D.I. Stroe, Unravelling and quantifying the aging processes of commercial $Li(Ni_{0.5}Co_{0.2}Mn_{0.3})O_2$/graphite lithium-ion batteries under constant current cycling, J. Mater. Chem. A 11 (2022) 41–52, https://doi.org/10.1039/d2ta05960f.
[4] W. Mei, L. Jiang, C. Liang, J. Sun, Q. Wang, Understanding of Li-plating on graphite electrode: detection, quantification and mechanism revelation, Energy Storage Mater. 41 (2021) 209–221, https://doi.org/10.1016/j.ensm.2021.06.013.
[5] J. Deng, C. Bae, J. Marcicki, A. Masias, T. Miller, Safety modelling and testing of lithium-ion batteries in electrified vehicles, Nat. Energy 3 (2018) 261–266, https://doi.org/10.1038/s41560-018-0122-3.
[6] S.J. An, J. Li, C. Daniel, D. Mohanty, S. Nagpure, D.L. Wood, The state of understanding of the lithium-ion-battery graphite solid electrolyte interphase (SEI) and its relationship to formation cycling, Carbon N. Y. 105 (2016) 52–76, https://doi.org/10.1016/j.carbon.2016.04.008.
[7] L. von Kolzenberg, A. Latz, B. Horstmann, Solid–electrolyte interphase during battery cycling: theory of growth regimes, ChemSusChem 13 (2020) 3901–3910, https://doi.org/10.1002/cssc.202000867.
[8] C.Y. Wang, T. Liu, X.G. Yang, S. Ge, N.V. Stanley, E.S. Rountree, Y. Leng, B. D. McCarthy, Fast charging of energy-dense lithium-ion batteries, Nature 611 (2022) 485–490, https://doi.org/10.1038/s41586-022-05281-0.
[9] J. Li, R.G. Landers, J. Park, A comprehensive single-particle-degradation model for battery state-of-health prediction, J. Power Sources 456 (2020), https://doi.org/10.1016/j.jpowsour.2020.227950.
[10] X.G. Yang, Y. Leng, G. Zhang, S. Ge, C.Y. Wang, Modeling of lithium plating induced aging of lithium-ion batteries: transition from linear to nonlinear aging, J. Power Sources 360 (2017) 28–40, https://doi.org/10.1016/j.jpowsour.2017.05.110.
[11] C. von Lüders, J. Keil, M. Webersberger, A. Jossen, Modeling of lithium plating and lithium stripping in lithium-ion batteries, J. Power Sources 414 (2019) 41–47, https://doi.org/10.1016/j.jpowsour.2018.12.084.
[12] Y. Chen, L. Yang, F. Guo, D. Liu, H. Wang, J. Lu, J. Zheng, X. Yu, H. Li, Mechanical-electrochemical modeling of silicon-graphite composite anode for lithium-ion batteries, J. Power Sources 527 (2022), 231178, https://doi.org/10.1016/j.jpowsour.2022.231178.
[13] J.S. Edge, S. O'Kane, R. Prosser, N.D. Kirkaldy, A.N. Patel, A. Hales, A. Ghosh, W. Ai, J. Chen, J. Yang, S. Li, M.C. Pang, L. Bravo Diaz, A. Tomaszewska, M. W. Marzook, K.N. Radhakrishnan, H. Wang, Y. Patel, B. Wu, G.J. Offer, Lithium ion battery degradation: what you need to know, Phys. Chem. Chem. Phys. 23 (2021) 8200–8221, https://doi.org/10.1039/d1cp00359c.
[14] C. Yuan, Y. Hahn, W. Lu, V. Oancea, J. Xu, Quantification of electrochemical-mechanical coupling in lithium-ion batteries, Cell Rep. Phys. Sci. 3 (2022), 101158, https://doi.org/10.1016/j.xcrp.2022.101158.
[15] W. Ai, B. Wu, E. Martínez-Pañeda, A coupled phase field formulation for modelling fatigue cracking in lithium-ion battery electrode particles, J. Power Sources 544 (2022), 231805, https://doi.org/10.1016/j.jpowsour.2022.231805.
[16] Y. Bi, J. Tao, Y. Wu, L. Li, Y. Xu, E. Hu, B. Wu, J. Hu, C. Wang, J.G. Zhang, Y. Qi, J. Xiao, Reversible planar gliding and microcracking in a single-crystalline Ni-rich cathode, Science 370 (80-) (2020) 1313–1318, https://doi.org/10.1126/science.abc3167.
[17] J. Mao, W. Tiedemann, J. Newman, Simulation of temperature rise in Li-ion cells at very high currents, J. Power Sources 271 (2014) 444–454, https://doi.org/10.1016/j.jpowsour.2014.08.033.
[18] J. Li, Y. Cheng, M. Jia, Y. Tang, Y. Lin, Z. Zhang, Y. Liu, An electrochemical-thermal model based on dynamic responses for lithium iron phosphate battery, J. Power Sources 255 (2014) 130–143, https://doi.org/10.1016/j.jpowsour.2014.01.007.
[19] P. Ping, Q. Wang, Y. Chung, J. Wen, Modelling electro-thermal response of lithium-ion batteries from normal to abuse conditions, Appl. Energy 205 (2017) 1327–1344, https://doi.org/10.1016/j.apenergy.2017.08.073.
[20] S. chun Yang, Y. Hua, D. Qiao, Y. bo Lian, Y. wei Pan, Y. ling He, A coupled electrochemical-thermal-mechanical degradation modelling approach for lifetime assessment of lithium-ion batteries, Electrochim. Acta (2019) 326, https://doi.org/10.1016/j.electacta.2019.134928.
[21] X. Gao, P. He, J. Ren, J. Xu, Modeling of contact stress among compound particles in high energy lithium-ion battery, Energy Storage Mater. 18 (2019) 23–33, https://doi.org/10.1016/j.ensm.2019.02.007.
[22] X. Gao, W. Lu, J. Xu, Modeling framework for multiphysics-multiscale behavior of Si–C composite anode, J. Power Sources 449 (2020), 227501, https://doi.org/10.1016/j.jpowsour.2019.227501.
[23] W. Guo, Z. Sun, S.B. Vilsen, F. Blaabjerg, D.I. Stroe, Identification of mechanism consistency for LFP/C batteries during accelerated aging tests based on statistical distributions, ePrime Adv. Electr. Eng. Electron. Energy 4 (2023), https://doi.org/10.1016/j.prime.2023.100142.
[24] M. Dubarry, D. Howey, B. Wu, Enabling battery digital twins at the industrial scale, Joule (2023) 1–11, https://doi.org/10.1016/j.joule.2023.05.005.
[25] W. Guo, Z. Sun, S.B. Vilsen, J. Meng, D.I. Stroe, Review of "grey box" lifetime modeling for lithium-ion battery: combining physics and data-driven methods, J. Energy Storage 56 (2022), https://doi.org/10.1016/j.est.2022.105992.
[26] Y. Che, X. Hu, X. Lin, J. Guo, R. Teodorescu, Health prognostics for lithium-ion batteries: mechanisms, methods, and prospects, Energy Environ. Sci. 16 (2023) 338–371, https://doi.org/10.1039/d2ee03019e.
[27] Y. Li, J. Guo, K. Pedersen, L. Gurevich, D.-I. Stroe, Investigation of multi-step fast charging protocol and aging mechanism for commercial NMC/graphite lithium-ion batteries, J. Energy Chem. (2023), https://doi.org/10.1016/j.jechem.2023.01.016.
[28] W. Guo, Y. Li, Z. Sun, S.B. Vilsen, D.-I. Stroe, Solid electrolyte interface layer growth - crack formation coupled model for Lithium-ion battery capacity fade prediction, in: Proceedings of the European Conference on Power Electronics and Applications, IEEE, 2023.
[29] A. Wang, S. Kadam, H. Li, S. Shi, Y. Qi, Review on modeling of the anode solid electrolyte interphase (SEI) for lithium-ion batteries, Npj Comput. Mater. (2018) 4, https://doi.org/10.1038/s41524-018-0064-0.
[30] W. Zhu, P. Zhou, D. Ren, M. Yang, X. Rui, C. Jin, T. Shen, X. Han, Y. Zheng, L. Lu, M. Ouyang, A mechanistic calendar aging model of lithium-ion battery considering solid electrolyte interface growth, Int. J. Energy Res. 46 (2022) 15521–15534, https://doi.org/10.1002/er.8249.
[31] H. Ekström, G. Lindbergh, A model for predicting capacity fade due to SEI formation in a commercial graphite/$LiFePO_4$ cell, J. Electrochem. Soc. 162 (2015) A1003–A1007, https://doi.org/10.1149/2.0641506jes.
[32] J. Li, K. Adewuyi, N. Lotfi, R.G. Landers, J. Park, A single particle model with chemical/mechanical degradation physics for lithium ion battery state of health (SOH) estimation, Appl. Energy 212 (2018) 1178–1190, https://doi.org/10.1016/j.apenergy.2018.01.011.
[33] Y.T. Cheng, M.W. Verbrugge, Evolution of stress within a spherical insertion electrode particle under potentiostatic and galvanostatic operation, J. Power Sources 190 (2009) 453–460, https://doi.org/10.1016/j.jpowsour.2009.01.021.
[34] P. Barai, K. Smith, C.F. Chen, G.H. Kim, P.P. Mukherjee, Reduced order modeling of mechanical degradation induced performance decay in lithium-ion battery porous electrodes, J. Electrochem. Soc. 162 (2015) A1751–A1771, https://doi.org/10.1149/2.0241509jes.

[35] W. Li, D. Cao, D. Jöst, F. Ringbeck, M. Kuipers, F. Frie, D.U. Sauer, Parameter sensitivity analysis of electrochemical model-based battery management systems for lithium-ion batteries, Appl. Energy 269 (2020), 115104, https://doi.org/10.1016/j.apenergy.2020.115104.

[36] J. Guo, Y. Li, J. Meng, K. Pedersen, L. Gurevich, D.I. Stroe, Understanding the mechanism of capacity increase during early cycling of commercial NMC/graphite lithium-ion batteries, J. Energy Chem. 74 (2022) 34–44, https://doi.org/10.1016/j.jechem.2022.07.005.

[37] N. Paul, M. Wetjen, S. Busch, H. Gasteiger, R. Gilles, Contrast matched SANS for observing SEI and pore clogging in silicon-graphite anodes, J. Electrochem. Soc. 166 (2019) A1051–A1054, https://doi.org/10.1149/2.0781906jes.

[38] M. Gaberšček, Understanding Li-based battery materials via electrochemical impedance spectroscopy, Nat. Commun. 12 (2021) 19–22, https://doi.org/10.1038/s41467-021-26894-5.

[39] M.T.F. Rodrigues, F.N. Sayed, H. Gullapalli, P.M. Ajayan, High-temperature solid electrolyte interphases (SEI) in graphite electrodes, J. Power Sources 381 (2018) 107–115, https://doi.org/10.1016/j.jpowsour.2018.01.070.